



**HAL**  
open science

## **In-depth characterisation of a mixture composed of powder/pellets MX80 bentonite**

Agustín Molinero Guerra, Nadia Mokni, Pierre Delage, Yu-Jun Cui, Anh Minh A.M. Tang, Patrick Aimedieu, Frédéric Bernier, Michel Bornert

► **To cite this version:**

Agustín Molinero Guerra, Nadia Mokni, Pierre Delage, Yu-Jun Cui, Anh Minh A.M. Tang, et al.. In-depth characterisation of a mixture composed of powder/pellets MX80 bentonite. *Applied Clay Science*, 2017, 135, pp.538-546. 10.1016/j.clay.2016.10.030 . hal-01515960v2

**HAL Id: hal-01515960**

**<https://enpc.hal.science/hal-01515960v2>**

Submitted on 29 Jan 2021

**HAL** is a multi-disciplinary open access archive for the deposit and dissemination of scientific research documents, whether they are published or not. The documents may come from teaching and research institutions in France or abroad, or from public or private research centers.

L'archive ouverte pluridisciplinaire **HAL**, est destinée au dépôt et à la diffusion de documents scientifiques de niveau recherche, publiés ou non, émanant des établissements d'enseignement et de recherche français ou étrangers, des laboratoires publics ou privés.



Distributed under a Creative Commons Attribution - NonCommercial - NoDerivatives 4.0 International License

# In-depth characterisation of a mixture composed of powder/pellets MX80 bentonite

Agustín Molinero Guerra<sup>1,2</sup>, Nadia Mokni<sup>2</sup>, Pierre Delage<sup>1</sup>, Yu-Jun Cui<sup>1</sup>, Anh Minh Tang<sup>1</sup>,  
Patrick Aïmedieu<sup>1</sup>, Frédéric Bernier<sup>3</sup>, Michel Bornert<sup>1</sup>

<sup>1</sup>Ecole des Ponts ParisTech, Laboratoire Navier, Marne la Vallée, France

<sup>2</sup>Institut de Radioprotection et de Sûreté Nucléaire (IRSN), Fontenay-aux-Roses, France

<sup>3</sup>Agence Fédérale de Contrôle Nucléaire (AFCN), Belgique

**Abstract:** Mixtures made up of bentonite powder and pellets are a possible candidate for making sealing plugs used in deep radioactive waste disposal due to their low permeability, high swelling capacity, favourable properties with respect to radionuclide retention and operational advantages in terms of placement *in situ*, that is much easier than that of pre-compacted bricks of bentonite/sand mixture. It is therefore essential to better understand their hydro-mechanical behaviour to optimize the design of the repository. In this context, the French Institute for Radiation Protection and Nuclear Safety (IRSN) has launched the SEALEX project (SEALing performance EXperiments) in which this work has been conducted.

Once the initially heterogeneous unsaturated powder/pellet (80/20) MX80 bentonite mixture is put in place, these sealing materials will be subject to coupled hydro-mechanical loadings: hydration due to the infiltration of pore water from the natural barrier and mechanical confinement resulting from the engineered barriers. The present work focuses on the different scales of the material: at the macroscopic scale, it is characterized by a heterogeneous distribution of pellets and powder of bentonite; at the microscopic scale, it is studied by several techniques (MIP,  $\mu$ -CT observations and SEM). From MIP results, a typical bimodal distribution was found for both pellet and powder. From  $\mu$ -CT and SEM observations, a heterogeneity was revealed in the internal structure of the pellet: heterogeneous density distribution of the clay minerals and presence of several high density elements.

**Keywords:** heterogeneous pellet/powder bentonite mixture; sealing plug; radioactive waste disposal; microstructure; mercury intrusion porosimetry; X-ray computed microtomography; scanning electron microscopy.

## 37 **1. Introduction**

38 In the French concept of deep geological disposal for High Level and Intermediate Level  
39 Long Lived radioactive Wastes (HLW & ILLW), the wastes are emplaced within large  
40 diameter boreholes (HLW) and galleries (ILLW) excavated at great depths in a low-  
41 permeability host-rock (Callovo-Oxfordian argillite, ANDRA, 2005). Sealing of these  
42 underground works to prevent potential pathways for water, gas and radionuclides migration  
43 is one of the key points to ensure the long-term safety of the repository.

44 Mixtures made up of bentonite powder and pellets are a candidate sealing material for deep  
45 underground radioactive waste repositories. In addition to their low permeability, high  
46 swelling capacity and high radionuclide migration retardation properties, powder/pellet  
47 mixtures have obvious operational advantages in terms of emplacement and reduction of the  
48 gaps between the rock and the seal. Once installed in the repository, powder/pellet mixtures  
49 will be submitted to coupled hydro-mechanical loadings comprising hydration due to the  
50 infiltration of pore water from the host rock and mechanical confinement resulting from the  
51 constrained volume condition imposed in the galleries. It is therefore essential to better  
52 understand their hydro-mechanical behaviour when assessing the overall repository safety.

53 In this context, and as part of the overall IRSN (French Institute for Radiological Protection  
54 and Nuclear Safety) R&D program that provides scientific background for its expertise on  
55 disposal safety, the SEALEX (SEALing performance Experiments) project was launched to  
56 specifically focus on long-term performance of sealing systems. The SEALEX project is  
57 dedicated (i) to test the long-term hydraulic performance of sealing systems in normal  
58 conditions for different core compositions (mixtures composed of bentonite pellets with  
59 bentonite powder or of sand with bentonite powder) and for different configurations (pre-

60 compacted bentonite blocks or bentonite compacted *in situ*), (ii) to quantify the impact of  
61 construction joints (also called technological voids) on the hydraulic properties of the sealing  
62 system, and (iii) investigate the concept of robustness by considering altered scenarios, such  
63 as an incidental decrease of the swelling pressure (for instance originating from the failure of  
64 the confining plugs). This project relies on a series of *in situ* experiments emplaced in IRSN's  
65 Underground Research Laboratory (URL) at Tournemire located in a Mesozoic sedimentary  
66 basin on the western edge of the French Causses (South France) (Mokni & Barnichon., 2016).  
67 To install the experiments, horizontal boreholes ( $0 \pm 2^\circ$ ), with a 60 cm diameter and 540 cm  
68 long have been excavated from recent drifts (2008). Each experiment consists of a bentonite-  
69 based core mechanically confined at both ends corresponding to a generic seal mock-up  
70 except in terms of saturation that will be an artificial one carried out by water injection  
71 through porous filters installed at both ends of the core (Barnichon et al., 2012; Mokni &  
72 Barnichon., 2016). Various materials are being considered as seals in the SEALEX project.  
73 The present work focuses on a mixture made up of MX80 bentonite powder and pellets with a  
74 proportion of 20/80 in dry mass.

75 The use of high-density bentonite pellets combined with bentonite powder has also been  
76 proposed in Salo & Kukkola (1989), Dereeper et al. (2001), Ab (2002). A characterisation of  
77 the fundamental properties of the MX80 bentonite pellets used in the Prototype Repository  
78 test is reported in Sugita et al. (2005). At a larger scale, a series of infiltration tests on a  
79 50/50% FoCa bentonite pellet/powder mixture compacted at different dry densities were  
80 performed by Imbert & Villar (2006) to investigate the swelling capacity of the material.

81 It is well documented that the macroscopic behaviour of expansive soils is related to its  
82 microstructure (e.g. Alonso et al., 2011; Gens & Alonso, 1992). For this reason, several  
83 investigations have been carried out on the microstructure of bentonite-based materials by  
84 using several methods including Mercury Intrusion Porosimetry (MIP) and/or Scanning

85 Electron Microscopy (SEM) (Wang et al., 2012, 2013, 2014; Saba et al., 2014; Romero et al.,  
86 2011). There is less available data on pellets and powder-pellets mixtures. Hoffmann (2005)  
87 carried out MIP tests on samples of pellets of FEBEX bentonite under different conditions  
88 and observed a bimodal distribution on a single pellet with a dry unit mass  $\rho_d = 1.95 \text{ Mg/m}^3$ .  
89 For a non-compacted pellet mixture, a trimodal distribution was identified with two  
90 populations of pores corresponding to the intra and inter-aggregate pores and the third one  
91 related to the inter-pellet pores.

92 The microstructure investigation techniques require a preliminary dehydration of the samples,  
93 often carried out by freeze-drying. Due to the size of the sample investigated, these techniques  
94 provide local observations of a part of millimetric samples. These results may fruitfully be  
95 complemented by the use of X-ray computed microtomography ( $\mu$ -CT), a non-destructive 3D  
96 technique that provides high-resolution observations of samples at a larger scale without any  
97 pre-treatment. The changes in microfabric during hydration under constant volume conditions  
98 of a 50/50 pellet/powder mixture of FoCa clay at a dry unit weight of  $1.36 \text{ Mg/m}^3$  were  
99 observed by Van Geet et al. (2005) using  $\mu$ -CT. The significant changes of the pellet/powder  
100 mixture during hydration could be observed but the technique did not allow investigating the  
101 microstructure of an elementary pellet itself because the resolution of the images obtained was  
102 not enough in order to study the material at this scale.

103 This paper deals with an experimental program aiming to study the microstructural features of  
104 a pellet/powder mixture at various scales by using  $\mu$ -CT observations coupled to MIP and  
105 SEM investigations. This mixture will afterwards be used to develop a mock-up test in the  
106 laboratory, to simulate SEALEX *in situ* tests at reduced scale (1/10) by considering a column  
107 of 60 mm in diameter and 120 mm in height.

## 108 **2. Materials and methods**

## 109        **2.1. Materials**

110    The materials investigated are on the one hand the basic pellet made of MX80 bentonite and  
111    on the other hand a mixture of MX80 bentonite powder and pellets at a proportion of 20/80 in  
112    dry mass (Figure 1). The bentonite used comes from Wyoming, USA, and was provided by  
113    the Laviosa-MPC company under the commercial name Expangel (Expangel SP7 for pellets  
114    and Expangel SP32 for the powder). To make things clear, the name MX80 will however be  
115    used here. The MX80 bentonite has a high smectite content (80%) with some inclusions of  
116    non-clayey minerals (see Table 1) and a cation exchange capacity (CEC) of 98 meq/100g. The  
117    major exchangeable cation is  $\text{Na}^+$ , with a value of 52 meq/100g (Table 2). The liquid limit is  
118    560%, the plastic limit is 53% and the unit mass is of  $2.77 \text{ Mg/m}^3$  (Saba et al., 2014, Table 3).  
119    Pellets were industrially produced in Laviosa-MPC company by instantaneously compacting a  
120    powder of MX80 bentonite in a mould of 7 mm of diameter and 7 mm of height (Laviosa  
121    Minerals). The fabrication was done at water content  $w = 5\% - 7\%$  and at dry unit mass  $\rho_d =$   
122     $1.998 \text{ Mg/m}^3 - 2.12 \text{ Mg/m}^3$ . Pellets were received in packages of 25 kg and stored in the  
123    laboratory at  $20^\circ\text{C}$ . The pellet initial suction was measured in the laboratory with a chilled  
124    mirror dew point tensiometer (Decagon WP4), providing a value  $s = 132.4 \text{ MPa}$  at initial  
125    water content  $w = 7.25\%$  (determined after drying in the oven at  $105^\circ\text{C}$  during 24h). More  
126    details about the initial properties of the pellets and the powder are presented in Table 3.  
127    Figure 2 shows a typical pellet with a radius of 7.14 mm and a height of 7.27 mm. It appears  
128    that the pellet has a quasi-cylindrical shape with two spherical poles on top and bottom. The  
129    lengths measured in the laboratory were larger than those just after the fabrication (7 mm),  
130    indicating swelling due to hydration in the course of storage. Indeed, higher water contents  
131    (7.25% - 6.69%) were measured on pellets located at the top of the bucket stored in the  
132    laboratory, compared to that located at the bottom (6.06% - 6.00%).

133 The MX80 bentonite powder was produced by crushing pellets. The characteristics at initial  
134 state is presented in Table 3. Compared to the fabrication value of water content (between 5%  
135 and 7%), a value of 3.17% was found in the laboratory (after drying at 105°C for 24h)  
136 corresponding to an initial suction  $s = 190.9$  MPa, measured with a chilled mirror dew point  
137 tensiometer (Decagon WP4). The grain size distribution of the powder, obtained by dry  
138 sieving is presented in Figure 3 together with the size of a pellet. The average diameter is  
139  $D_{50} = 0.65$  mm.

140

## 141 **2.2. Testing procedures**

### 142 *Mercury intrusion porosimetry (MIP)*

143 The pore size distribution of both pellet and powder of MX80 bentonite was obtained on  
144 freeze dried samples using an Autopore IV 9500 mercury intrusion porosimeter  
145 (Micromeritics) that operates at a maximum pressure of 230 MPa. Instantaneous freezing was  
146 carried out by plunging small samples (a pellet of bentonite) in slush nitrogen (-210°C)  
147 obtained by previously submitting it to vacuum (Delage et al., 1996). In such conditions, there  
148 is no nitrogen boiling around the samples when plunging them into nitrogen, resulting in an  
149 optimized quick freezing and good microstructure preservation. The pore size distribution was  
150 obtained assuming parallel, cylindrical nonintersecting pores of different radii, using the  
151 Autopore IV 9500 V1.09 standard software package. The total void ratio was obtained by  
152 standard methods and compared to the total volume of mercury intruded into the sample at a  
153 pressure of 230 MPa.

### 154 *X-ray computed microtomography ( $\mu$ -CT)*

155 The  $\mu$ -CT scans were carried out using an “Ultratom” microtomograph (RX Solutions,  
156 France). Images were reconstructed using the software Xact (RX Solutions). The source is a

157 microfocus X-ray tube Hamamatsu L10801 and the imager is a Paxscan Varian 2520V  
158 (1960x1536 square pixels 127 $\mu$ m in size).

159 Several  $\mu$ -CT observations were carried out on a pellet of bentonite at initial state and on the  
160 powder/pellet MX80 bentonite mixture with a proportion of 80/20 in dry mass. For a single  
161 pellet of bentonite, the X-ray source parameters were 80 kV and 40  $\mu$ A; the voxel size was  
162 4.4  $\mu$ m. The samples were scanned using 1440 projections equally spread on 360°. After  
163 reconstruction, 1292 horizontal slices were calculated (16bit images; 1644x1292 pixels). For  
164 the powder/pellet mixture, the X-ray source parameters were 100 kV and 25  $\mu$ A; the voxel  
165 size was 59  $\mu$ m. The mixture was scanned using 2880 projections in helical mode and after  
166 reconstruction 2472 horizontal slices were obtained (16 bit images, 1735x1735 pixels).

167 *Scanning electron microscopy (SEM) and Energy-Dispersive X-ray spectroscopy (EDS)*

168 SEM combined to EDS was performed in order to carry out a chemical characterization of a  
169 pellet of bentonite at initial state. Instantaneous freezing was carried out by plunging the  
170 samples in slush nitrogen (-210°C). After freeze-drying, the pellet of bentonite was carefully  
171 cut at mid-height, separating the upper and the lower poles. Once cut, the specimens were  
172 immersed into a resin and polished with abrasive papers with decreasing fineness from grade  
173 800 to 4000 in order to obtain a smooth surface. Finally, the samples were metallized under  
174 vacuum with gold and palladium. Observations in conventional SEM require a high vacuum  
175 condition to allow a precise focusing of the incident electrons on the sample and to prevent  
176 the emitted electrons from interacting with the atmosphere.

### 177 **2.3. The pellet/bentonite mixture**

178 Two SEALEX performance tests with core made of MX80 bentonite powder/pellets (20/80)  
179 have been installed in Tournemire URL, in February and October 2013, to investigate the  
180 impact of core composition and conditioning on the long term performance of sealing



181 systems. To ensure the feasibility of injecting within a large diameter and compacting *in situ* a  
182 seal made of pellet/powder mixture so as to obtain a reasonably homogeneous core with the  
183 target dry unit mass of  $1.49 \text{ Mg/m}^3$ , a series of preliminary full scale mock up tests were  
184 carried out using a plastic tube with transparent windows to allow the observation of the  
185 distribution of the mixture within the emplacement borehole. The bentonite was introduced by  
186 means of an auger conveyor measuring 5 m in length and 60 mm in outer diameter. The auger  
187 measures 50 mm in diameter and is driven by a 1.5 kW geared motor. The tube features a  
188 loading hopper and has a flanged connection in its midpoint, so that despite its length it can be  
189 easily mounted in the gallery with its back end already inserted in the borehole, as the auger  
190 inside is flexible.

191 It is however important to prepare an homogeneous powder/pellet MX80 bentonite mixture at  
192 the required target dry unit mass ( $1.49 \text{ Mg/m}^3$ ) because the dry unit mass governs both the  
193 saturated permeability ( $k_w$ ) and the swelling pressure of the mixture (Saba et al., 2014;  
194 Hoffmann et al., 2007). In this study, the challenge was to obtain a reasonably homogeneous  
195 powder/pellet mixture to be placed in a reduced scale mock-up test of the SEALEX *in situ*  
196 tests. This mock-up test is planned to be carried out at a scale of 1/10 of the SEALEX tests,  
197 corresponding to a cylinder of 60 mm in diameter and 120 mm in height.

198 Three protocols were considered aiming at identifying the one that provides the best  
199 homogeneity. The first protocol consisted in filling the cell by packets corresponding to one  
200 layer of pellets spread over the base of the 60 mm diameter cylinder and by adding the  
201 corresponding amount of powder (80% pellets and 20% powder). The second protocol was  
202 comparable but involved two layers of pellets. Finally, the third protocol consisted in filling a  
203 quantity of pellets corresponding to three layers, but that has been previously mixed with the  
204 powder.

205

## 206        **3. Results**

### 207        **3.1. X-ray computed microtomography**

#### 208        *Case of Pellet*

209        Further information about the microstructure of a pellet of bentonite at initial state (suction  $s$   
210        = 132.4 MPa, water content  $w = 7.25\%$  and dry unit mass  $\rho_d = 2.12 \text{ Mg/m}^3$ ) was obtained  
211        using  $\mu$ -CT observations.

212        Figure 4 and Figure 5 show horizontal and vertical slices, respectively, taken at different  
213        positions as indicated in the photo of the pellets presented on top left in the figures. Grey  
214        levels depend on the density and atomic number of the components, with darker grey levels  
215        typically corresponding to lower densities and black zones to voids. Several higher density  
216        elements (light grey levels) are observed in both cases. Several cracks are identified in the  
217        sections located in the upper part of the pellet (horizontal sections I and II, and vertical  
218        sections I, II and III). It can be deduced from Figure 4 that they coincide with the upper  
219        spherical part, close to the contact with the cylindrical section. Such fissures are not observed  
220        on the same zone at the bottom of the pellet.

221        Further information about the fissure network is obtained by a 3D rendering of the surfaces  
222        defined by the cracks within a region of interest of the pellet at initial state presented in Figure  
223        6. Cracks are defined as the voxels with a grey level below some threshold. It is observed that  
224        crack networks are located on both the upper and bottom part of the pellet; however, as it was  
225        revealed by horizontal and vertical slices, there are more cracks in the upper part. The 3D  
226        rendering was performed by means of the Avizo image analysis software.

227        Further investigation on a single pellet and on the respective distribution of pellets and  
228        powder within the mixture was done by means of image analysis. In a first step, a region of  
229        interest (ROI) in the sample was selected (Figure 7). Then, a segmentation of the image was

230 made to separate the voids from the other phases (i.e. the pellets and the powder grains). This  
231 step was completed using the ImageJ image analysis software. This method is a variation of  
232 the IsoData algorithm (Ridler & Calvard, 1978), an iterative procedure that divides the image  
233 into an object and a background by adopting an initial threshold. Then the averages of the  
234 pixels at or below the threshold and pixels above are computed, the threshold is incremented  
235 and the process is repeated until the threshold is larger than the composite average. Figure 7  
236 shows the initial state with the selected ROI (a) and the segmented image (b). It is noted that  
237 such a procedure does not give access to an accurate evaluation of the actual total porosity of  
238 the sample, as the result strongly depends on the selected threshold, is strongly sensitive to  
239 partial volume effects and other image artefacts, and does not allow to detect the smaller  
240 pores. It provides however a way to characterize, at least qualitatively, the spatial distribution  
241 of the larger voids within the sample.

242

243 An investigation of the porosity was conducted on a single pellet of bentonite with this  
244 approach. The porosity was calculated for each horizontal slice obtained by  $\mu$ -CT  
245 observations by dividing the number of black voxels (below some threshold, corresponding to  
246 voids) by the total number of voxels within the pellet. Figure 8 and Figure 9 present the  
247 calculated values of void ratio for horizontal and vertical sections respectively. It is confirmed  
248 from Figure 8 that the value of void ratio increases at the upper part of the pellet (for a level  
249 higher than 5 mm) because of the presence of the fissures. In Figure 9 (calculated void ratio  
250 for each vertical section), the highest values of void ratio are located at both edges and in the  
251 centre of the pellet. Note that this porosity corresponds to that detected by image analysis with  
252 a resolution of 4.4  $\mu\text{m}/\text{voxel}$  and for a particular choice of grey level threshold; hence, it  
253 provides a first evaluation of the porosity associated with the cracks (see for instance the 3D  
254 representation of the fissure network of Figure 6).

255

256 *Case of Pellet-powder mixture*

257 The homogeneity of the specimens obtained by using each of the three protocols was  
258 examined by using X-ray computed microtomography, the results of which are presented in  
259 Figure 10. Observation of Figure 10a shows that the first protocol (1 layer) provided a  
260 reasonably good homogeneity of the mixture, with regular scattering of the powder grains  
261 within the pores located between the pellets. Several voids between the pellets are however  
262 observed at the top of the sample. Inspection of Figure 10b shows that the homogeneity is not  
263 ensured with the second protocol (2 layers) with much more inter-pellets pores that are not  
264 filled with powder, particularly in the peripheral part of the specimen. Note also the presence  
265 of large inter-pellets voids completely filled with powder, in the middle of the sample at 1/3  
266 of the height. The same problem is observed with the third protocol (Figure 10c). The target  
267 dry unit mass ( $\rho_d = 1.49 \text{ Mg/m}^3$ ) was obtained with the first protocol only, while a unit mass  
268 of  $\rho_d = 1.41 \text{ Mg/m}^3$  and  $1.43 \text{ Mg/m}^3$  is found for the second and third protocols respectively.

269

270 An investigation of the porosity was conducted on the three protocols in the same way as  
271 detailed previously for a single pellet of bentonite. To this end, the porosity was estimated for  
272 each horizontal slice obtained by  $\mu$ -CT observations, using the same threshold for all slices.  
273 Figure 11 presents the evolution of the obtained porosity along the height of the sample for  
274 the three protocols. One can observe an oscillation of the value of porosity for all three  
275 protocols. In the first one, the minimum and maximum void ratios are 0.18 and 0.63  
276 respectively. Oscillations are more remarkable and they correspond to one layer of pellets. In  
277 the second protocol, the minimum and maximum void ratio values are 0.15 and 0.33  
278 respectively, oscillating around a value of 0.2. Finally, for the third protocol, void ratio goes  
279 from 0.08 to 0.55, and the oscillations correspond to three layers of pellets.

280

281 Taking into account the target dry density, the homogeneity observed in Figure 10 and the  
282 data of image analysis, the first protocol should be selected in order to prepare the  
283 pellet/powder mixture samples of MX80 bentonite. Note however that the best result  
284 corresponds to the second protocol according to the image analysis, because the values of  
285 void ratio oscillate around a value of 0.2 for all the sections. This low fluctuation along the  
286 vertical direction of the apparent average porosity within a section does however not reflect  
287 the strong heterogeneity of the pore distribution within a section, which is observed in the  
288 vertical slice represented in Figure 12b. Furthermore, the target dry density ( $1.49 \text{ Mg/m}^3$ ) was  
289 only obtained with the first protocol.

290

### 291 **3.2. Mercury intrusion porosimetry**

292 Figure 12 shows the results of MIP tests carried out on a pellet ( $w = 6.7\%$ ,  $s = 138.4 \text{ MPa}$ )  
293 and on the bentonite powder ( $w = 3.1\%$ ,  $s = 190.9 \text{ MPa}$ ). The cumulative curve (Figure 12a)  
294 shows that the final value of intruded mercury void ratio of the pellet ( $e = 0.23$ ) is lower than  
295 its total void ratio ( $e_T = 0.34$ ), indicating a significant porosity with an average diameter  
296 smaller than 5.5 nm, corresponding to the maximum mercury pressure applied (230 MPa).  
297 This is well known for compacted smectite (Lloret et al., 2003; Delage et al., 2006; Ridley et  
298 al., 2010).

299 A typical bimodal porosity distribution is observed for the bentonite powder, with an intruded  
300 void ratio of 0.9 at maximum mercury pressure (230 MPa). Actually, this void ratio is  
301 conditioned by the isotropic compression exerted by the mercury prior to penetrating the  
302 powder. The density function curve indicates that this penetration occurs at an average  
303 entrance diameter of 207  $\mu\text{m}$  between powder grains with an average diameter of 0.65 mm.

304 This configuration is not far from the standard ratio between the diameter of spherical grains  
305 and the inter-grains pores of their dense assembly, known to be close to 1/3. The second pore  
306 population is defined by an average entrance of 16.6 nm, to relate to a suction of 190.9 MPa  
307 of the powder.

308 The PSD curve of the pellet has a population of micro-pores quite comparable with an  
309 average entrance diameter of 13.3 nm, recalling that the powder was obtained from crushed  
310 pellets. Another less clearly defined porosity is observed with an average entrance diameter of  
311 5  $\mu\text{m}$ , that will be described in more details later on. The intruded void ratio represents 67.6%  
312 of the total void ratio. The void ratio of the population of large pores represents around 5.6%  
313 of the total void ratio.

### 314 **3.3. EDS characterisation**

315 Figure 13 presents SEM photos along with the corresponding EDS chemical analysis of the  
316 inclusions of different minerals observed within the pellet of bentonite. These inclusions  
317 correspond to the high density elements found by  $\mu$ -CT observations and are included in the  
318 mineralogical composition of the MX80 bentonite given in Table 1. These minerals are  
319 identified based on the chemical composition detected by EDS: a high concentration of silicon  
320 indicate an inclusion of quartz (see the two inclusions observed in Figure 13a and b); a  
321 concentration in sulphur/iron indicate a pyrite inclusion (see Figure 13c). Note that the  
322 dimensions of these inclusions are significant (137.3  $\mu\text{m}$  and 70.4  $\mu\text{m}$  for the quartz  
323 inclusions) compared to the size of the pellet. An inclusion of calcite is also observed in  
324 Figure 14, which was not identified in the X-ray diffractometer (XRD) analyses of MX80  
325 bentonite (Table 1).

326

## 327 **4. Discussion**

328 Most of the investigations carried out up to now on bentonite-based materials have been based  
329 on the use of MIP and SEM (e.g. Saba et al., 2014; Wang et al., 2013, 2014; Romero et al.,  
330 2011). These techniques, that require preliminary dehydration of the samples and that concern  
331 specimen volumes smaller than about  $1 \text{ cm}^3$  can be fruitfully complemented by more recent  
332 techniques like X-ray computed microtomography (Van Geet et al., 2005) that investigate  
333 specimens at larger scale and do not require any preliminary treatment.

334 In this paper, the microstructure of a pellet of bentonite at its initial state was studied by the  
335 pore size distribution curve, obtained by MIP technique. An expected bimodal distribution  
336 was obtained, where, theoretically, micro-pores correspond to voids inside an aggregate of  
337 bentonite and macro-pores are related to pores between aggregates. The difference between  
338 the final value of intruded mercury and the total void ratio in the cumulative curves (Figure  
339 12) suggests that there are several void sizes which cannot be filled by mercury. These voids  
340 correspond to pores with a diameter smaller than 5.5 nm and large fissures identified by  $\mu$ -CT  
341 observations. Consequently, it would be convenient to complete this MIP results with  
342 nitrogen gas adsorption (BET) technique in future investigations. The PSD curve of the  
343 powder of bentonite at its initial state was also obtained. The micro-pores of a single pellet  
344 and that of the powder are similar. For the macro-pores, the mean entrance is much larger  
345 than the obtained value for a pellet of bentonite. This value corresponds to the voids between  
346 grains of bentonite.

347 X-ray computed microtomography ( $\mu$ -CT) observations revealed fissures at the upper part of  
348 the pellet of bentonite (sections I and II presented in Figure 4 and sections I, II and III in  
349 Figure 5) as well as non-swelling elements which could influence the swelling potential of the  
350 material. For the section I in Figure 4, located at the upper spherical pole of the pellet, there is  
351 a predominant grey level with some deviations. At the border of the section an element of

352 high density (white) is distinguished. Furthermore, several fissures are observed, confirming  
353 that the pellet had already swollen during storage at the laboratory.

354 For section II (Figure 4), located at the upper part of the pellet, more fissures are observed at  
355 the edge of the pellet, as well as elements of high density (white pixels observed everywhere).

356 Based on those observations, the following remarks could be made: (i) pellets swell from the  
357 border to the centre (layers in contact with the atmosphere will swell, inducing fissures) and  
358 (ii) fissures observed at section I (Figure 4), located at the upper spherical pole of the pellet,  
359 could be due to the fabrication process combined to swelling.

360

361 For sections III and IV (Figure 4), located at the medium level and the lower spherical pole  
362 respectively, no more fissures are observed, but several elements of high density can still be  
363 identified. This suggests that the internal structure of a pellet of bentonite is not  
364 homogeneous. In addition to the existence of high density elements, different grey levels in  
365 the clayey part of the pellet are observed. The same conclusions can be extracted from the  
366 vertical sections I, II and III (Figure 5).

367

## 368 **5. Conclusion**

369 The  $\mu$ -CT investigation of the microstructure of a pellet of bentonite provided interesting  
370 complementary features that could not be identified by MIP and SEM observations.

371 Heterogeneous features were observed in the internal structure of the pellet, consisting in a  
372 heterogeneous density distribution of the clay minerals and in the presence of several high  
373 density elements. Furthermore, several fissures were observed at the upper pole of the pellet.

374 This heterogeneity of a single pellet was confirmed by SEM and EDS observations, where  
375 several inclusions of non-swelling elements were observed (quartz, pyrite and calcite). The



376 dimensions of these inclusions are not negligible, indicating that this could have an influence  
377 on the swelling potential of the pellet.

378 The MIP tests carried out on a pellet and powder of MX80 bentonite revealed some similarity  
379 between both materials, which is not surprising since the powder was fabricated by crushing  
380 pellets of bentonite. This similarity consisted on a double porosity and a comparable value of  
381 the mean size diameter of the micro-pores. The complementary information provided by  $\mu$ -  
382 CT observations evidenced that macro-pores found by MIP results are due to voids between  
383 fissures observed at the upper pole of the pellet and cracks observed at the top and the bottom.  
384 A difference is observed when comparing the final value intruded by mercury and the total  
385 void ratio in the cumulative curves, which corresponds to micro-pores with a diameter smaller  
386 than 5.5 nm and large fissures observed by  $\mu$ -CT observations on the upper part of the pellet.  
387 Thus, in order to have a good understanding of the microstructure of bentonite-based  
388 materials, it is important to carry out these complementary observations together with MIP,  
389 SEM + EDS results. The  $\mu$ -CT observations obtained from a pellet/powder bentonite mixture  
390 revealed a heterogeneous initial distribution of both materials within the sample. Thus, it can  
391 be concluded that this mixture is characterized by a double heterogeneity: at a microscopic  
392 level, a heterogeneous structure inside a pellet of bentonite, and at a macroscopic level, a  
393 heterogeneous distribution of pellets and powder. The investigation of this initial  
394 heterogeneity is important to understand the long-term evolution of the sealing for larger scale  
395 systems. Initially, the system is characterized by a heterogeneous distribution of dry density,  
396 so an anisotropic swelling will be attended. Future investigations should be conducted in  
397 order to study the heterogeneity of the material at the final state.

398

399

400

401

402

403

## 404 **References**

- 405 ANDRA, 2005, Dossier 2005 argile-Tome-evolution phénoménologique du stockage  
406 géologique.Rapport Andra no. C.RP.ADS.04.0025, France.
- 407 N. Mokni & J:D Barnichon, Hydro-mechanical analysis of SEALEX *in situ* tests- Impact of  
408 technological gaps on long term performance of repository seals. *Engineering Geology*, 205,  
409 pp. 81-92.
- 410 Alonso, E.E., Romero, E. & Hoffmann, C., 2011. Hydromechanical behaviour of compacted  
411 granular expansive mixtures: experimental and constitutive study. *Géotechnique*, 61(4),  
412 pp.329–344.
- 413 Barnichon, J.D., Dick, P. & Bauer, C., 2012. The SEALEX *in situ* experiments : Performance  
414 tests of repository seals. *Harmonising Rock Engineering and the Environment - Qian and*  
415 *Zhou (eds) Taylor and Francis Group, London*, pp.1391–1394.
- 416 Delage, P. et al., 2006. Ageing effects in a compacted bentonite: a microstructure approach.  
417 *Géotechnique*, 56(5), pp.291–304.
- 418 Delage, P. et al., 1996. Microstructure of a compacted silt. *Canadian Geotechnical Journal*,  
419 33, pp.150–158.
- 420 Dereeper, B. et al., 2001. Pellets/powder mixture of bentonite for backfill and sealing of HLW  
421 repositories. *Adachi, K., Fukue, M. (Eds.), Clay Science for Engineering. Balkema,*  
422 *Rotterdam*, pp.487–490.
- 423 Van Geet, M., Volckaert, G. & Roels, S., 2005. The use of microfocus X-ray computed  
424 tomography in characterising the hydration of a clay pellet/powder mixture. *Applied*  
425 *Clay Science*, 29(2), pp.73–87.
- 426 Gens, A. & Alonso, E.E., 1992. A framework for behavior of unsaturated expansive clays.  
427 *Canadian Geotechnical Journal*, 29, pp.1013–1032.
- 428 Hoffmann, C., Alonso, E.E. & Romero, E., 2007. Hydro-mechanical behaviour of bentonite  
429 pellet mixtures. *Physics and Chemistry of the Earth*, 32(8-14), pp.832–849.
- 430 Hoffmann Jauge, C.A., 2005. Caracterización hidromecánica de mezclas de pellets de  
431 bentonita. Estudio experimental y constitutivo. Available at:  
432 <http://www.tdx.cat/handle/10803/6235> [Accessed July 13, 2015].

- 433 Imbert, C. & Villar, M.V., 2006. Hydro-mechanical response of a bentonite pellets/powder  
434 mixture upon infiltration. *Applied Clay Science*, 32(3-4), pp.197–209.
- 435 Lloret, A. et al., 2003. Mechanical behaviour of heavily compacted bentonite under high  
436 suction changes. , (1), pp.27–40. Available at:  
437 <http://dx.doi.org/10.1680/geot.53.1.27.37258>.
- 438 Management Swedish Nuclear Fuel and Waste, 2002. Äspö Hard Rock Laboratory. Annual  
439 Report 2001.
- 440 Ridler, T.W. Calvard, S., 1978. Picture Thresholding Using an Iterative Slection Method.  
441 *IEEE Transactions on Systems, Man and Cybernetics*, 8(8), pp.630–632.
- 442 Ridley, a., Zdravkovic, L. & Monroy, R., 2010. Evolution of microstructure in compacted  
443 London Clay during wetting and loading. *Géotechnique*, 60(2), pp.105–119.
- 444 Romero, E., Della Vecchia, G. & Jommi, C., 2011. An insight into the water retention  
445 properties of compacted clayey soils. *Géotechnique*, 61(4), pp.313–328.
- 446 Saba, S., Romero, E., et al., 2014. *Hydro-mechanical behaviour of bentonite-sand mixture*  
447 *used as sealing materials in radioactive waste disposal galleries*. Université de Paris Est.
- 448 Saba, S., Barnichon, J.-D., et al., 2014. Microstructure and anisotropic swelling behaviour of  
449 compacted bentonite/sand mixture. *Journal of Rock Mechanics and Geotechnical*  
450 *Engineering*, 6(2), pp.126–132. Available at:  
451 <http://linkinghub.elsevier.com/retrieve/pii/S1674775514000158>.
- 452 Salo, J.-P. & Kukkola, T., 1989. Bentonite pellets, an alternative buffer material for spent fuel  
453 canister deposition holes. *Workshop “Sealing of Radioactive Waster Repositories”*.  
454 *Braunschweig*.
- 455 Sugita, Y., Chijimatsu, M. & Suzuki, H., 2005. Fundamental properties of bentonite pellet for  
456 Prototype Repository Project. In: *Alonso, E. E., Ledesma, A. (Eds.), Advances in*  
457 *Understanding Engineered Clay Barriers*. A. A. Balkema Publishers, Leiden, pp.293–  
458 299.
- 459 Wang, L., 2012. Micromechanical experimental investigation and modelling of strain and  
460 damage of argillaceous rocks under combined hydric and mechanical loads. Available at:  
461 <http://pastel.archives-ouvertes.fr/pastel-00794900>.
- 462 Wang, Q. et al., 2013. Hydraulic conductivity and microstructure changes of compacted  
463 bentonite/sand mixture during hydration. *Engineering Geology*, 164, pp.67–76.  
464 Available at: <http://dx.doi.org/10.1016/j.enggeo.2013.06.013>.
- 465 Wang, Q. et al., 2014. Time- and density-dependent microstructure features of compacted  
466 bentonite. *Soils and Foundations*, 54(4), pp.657–666.
- 467
- 468

469 **List of Tables**

470 Table 1. Results from the X-ray diffractometer (XRD) of the MX80 bentonite. The results are  
471 expressed as a percent of the total mass (Laviosa Minerals SpA) ..... 20  
472 Table 2. Cation exchange capacity (CEC) and original exchangeable cations of the MX80  
473 bentonite (Laviosa Minerals SpA) ..... 20  
474 Table 3. Initial properties and conditions of pellets and powder of bentonite ..... 20  
475 Table 4. Properties of powder of MX80 bentonite..... 20

477 **List of figures**

478 Figure 1. Mixture of MX80 bentonite powder and pellets with a proportion of 20/80 in dry mass..... 21  
479 Figure 2. Pellet of bentonite at initial state. Dry unit mass  $\rho_d = 2.12 \text{ Mg/m}^3$  ..... 21  
480 Figure 3. Grain size distribution of the MX80 bentonite powder..... 21  
481 Figure 4. X-ray computed microtomography ( $\mu$ -CT) observations - horizontal sections - of a pellet of  
482 bentonite at its initial state..... 22  
483 Figure 5. X-ray computed microtomography ( $\mu$ -CT) observations - vertical sections - of a pellet of  
484 bentonite at initial state..... 22  
485 Figure 6. 3D rendering of a pellet of bentonite at initial state (a) and of the crack network in a region  
486 of interest (b). ..... 23  
487 Figure 7. Horizontal slice with the selected ROI (a) and segmented image (b). ..... 23  
488 Figure 8. Evolution of the void ratio with height of a pellet of bentonite at initial state (Y direction –  
489 horizontal sections)..... 24  
490 Figure 9. Evolution of the void ratio of a pellet of bentonite at initial state (X direction – vertical  
491 sections)..... 24  
492 Figure 10. Vertical cross section of X-ray computed microtomography images of a mixture of  
493 powder/pellets of bentonite with a proportion of 20/80 in dry mass obtained by three different  
494 protocols. (a) First protocol of mixture, (b) Second protocol and (c) third protocol..... 25  
495 Figure 11. Evolution of the void ratio along height of a pellet/powder MX80 bentonite mixture (80/20)  
496 fabricated by three protocols. .... 25  
497 Figure 12. Cumulative porosity curve (a) and derivative curve (b) for a pellet and powder of bentonite  
498 at their initial state. .... 26  
499 Figure 13. SEM pictures taken on a pellet of bentonite at its initial state (132.38 MPa of suction) +  
500 EDS results. Mineral inclusions of quartz (a, b) and pyrite (c). Dry unit mass  $\rho_d = 2.12 \text{ Mg/m}^3$  ..... 27  
501 Figure 16. SEM picture taken on a pellet of bentonite at its initial state (132.38 MPa of suction) + EDS  
502 results. Mineral inclusion of calcite. Dry unit mass  $\rho_d = 2.12 \text{ Mg/m}^3$  ..... 28

503

504

505

506

507

508 Table 1. Results from the X-ray diffractometer (XRD) of the MX80 bentonite. The results are  
 509 expressed as a percent of the total mass (Laviosa Minerals SpA)

<i>Mineral</i>	<i>% of the total mass</i>
<i>Pyrite</i>	<1%
<i>Smectite</i>	80%
<i>Albite</i>	2%
<i>Anorthite</i>	8%
<i>Quartz</i>	4%
<i>Muscovite</i>	4%

510

511 Table 2. Cation exchange capacity (CEC) and original exchangeable cations of the MX80  
 512 bentonite (Laviosa Minerals SpA)

<i>Property</i>	
<i>CEC Capacity</i>	98 meq/100g
<i>Na conversion</i>	52 meq/100g
<i>K conversion</i>	1.2 meq/100g
<i>Mg conversion</i>	10 meq/100g
<i>Ca conversion</i>	37 meq/100g

513

514 Table 3. Initial properties and conditions of pellets and powder of bentonite

	<i>Pellet</i>	<i>Powder</i>
<i>Initial suction, <math>s_0</math></i>	132.4 MPa	190.9 MPa
<i>Initial water content, <math>w_0</math></i>	7.25%	3.17%
<i>Initial dry density, <math>\rho_0</math></i>	2.12 Mg/m <sup>3</sup>	
<i>Initial porosity, <math>\varphi_0</math></i>	0.25	
<i>Unit mass of bentonite particles, <math>\rho_s^*</math></i>	2.77 Mg/m <sup>3</sup>	

515 \*(Saba et al., 2014)

516

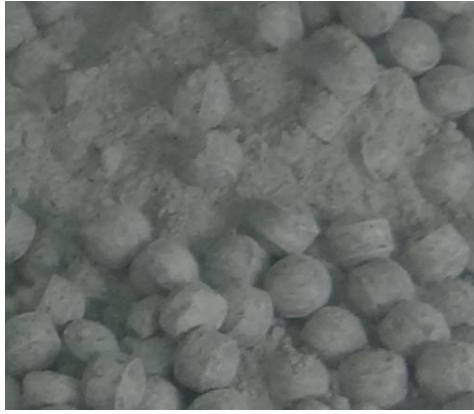
517 Table 4. Properties of powder of MX80 bentonite

<i>Atterberg limits</i>	
<i>Liquid limit, LL</i>	560%
<i>Plasticity limit, PL</i>	62%
<i>Shrinkage index, SI</i>	498%

518

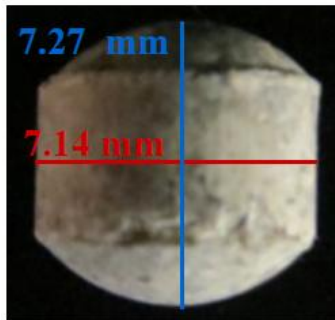
519

520



521 Figure 1. Mixture of MX80 bentonite powder and pellets with a proportion of 20/80 in dry  
522 mass.

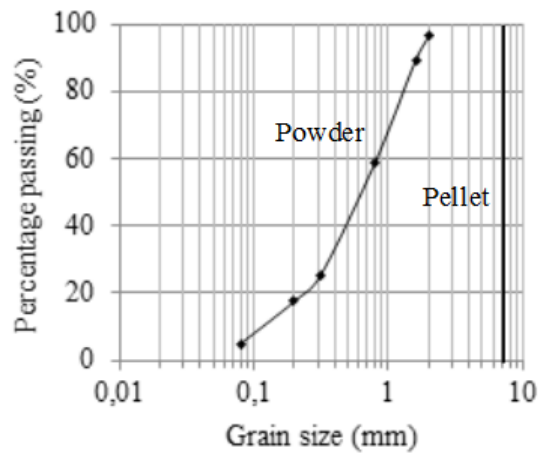
523



524

525 Figure 2. Pellet of bentonite at initial state. Dry unit mass  $\rho_d = 2.12 \text{ Mg/m}^3$

526



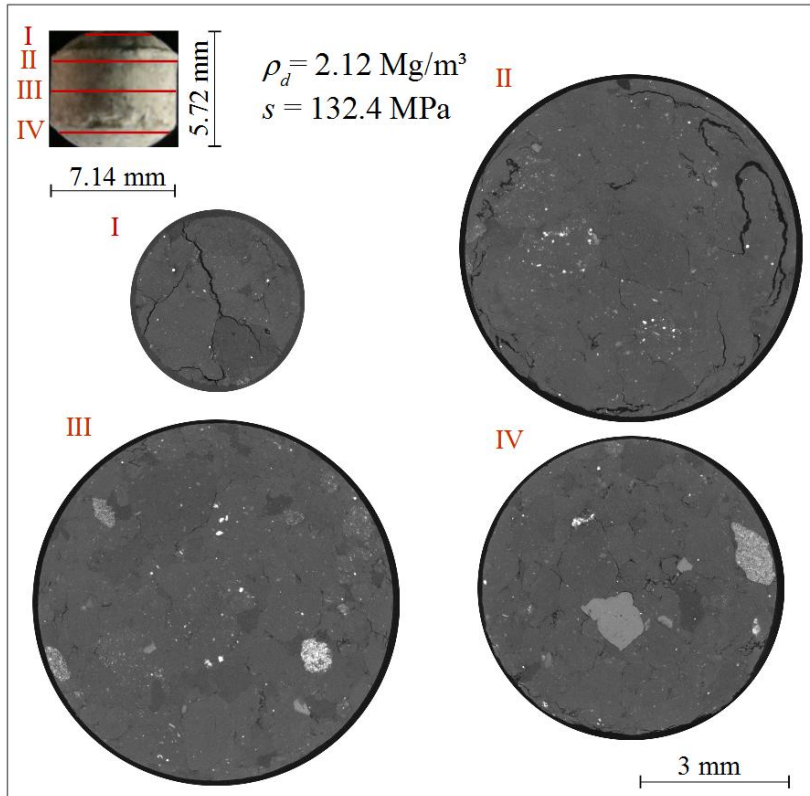
527

528 Figure 3. Grain size distribution of the MX80 bentonite powder.

529

530

531



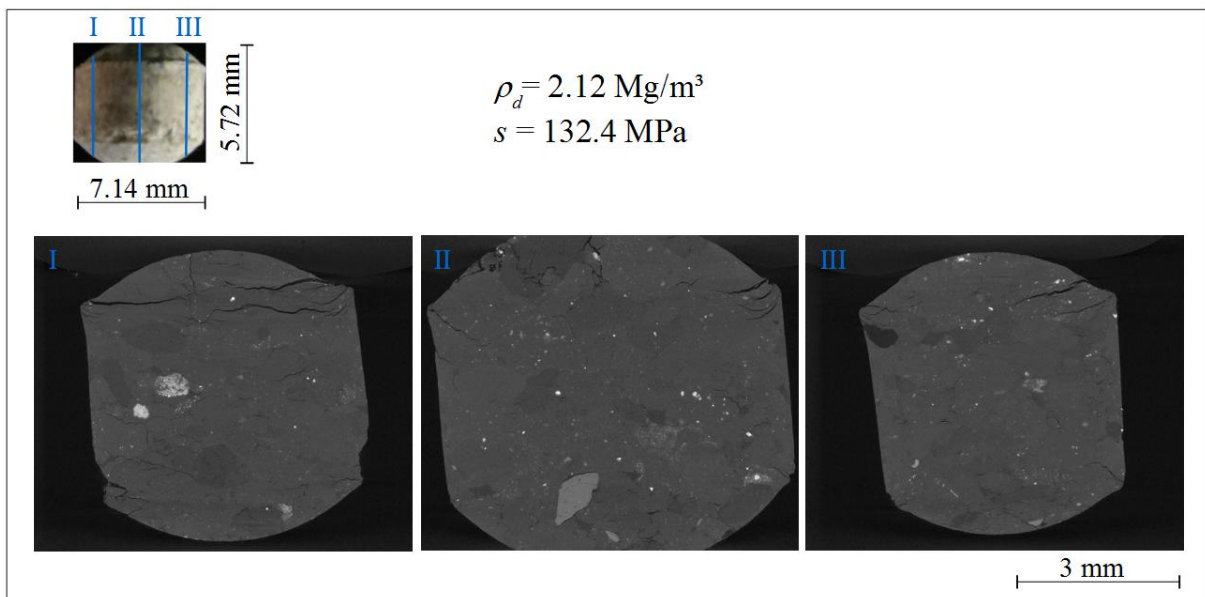
532

533

534

535

Figure 4. X-ray computed microtomography ( $\mu$ -CT) observations - horizontal sections - of a pellet of bentonite at its initial state.



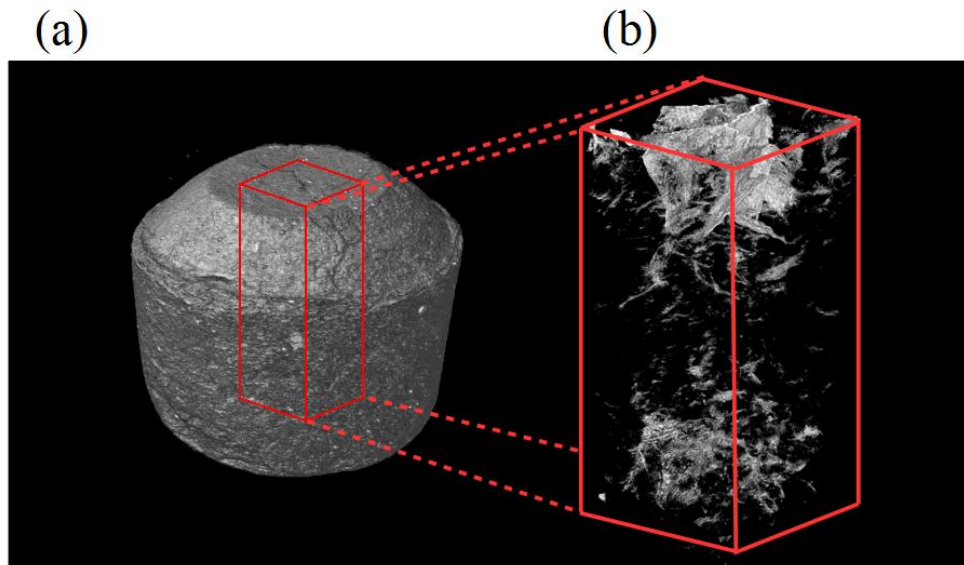
536

537

538

539

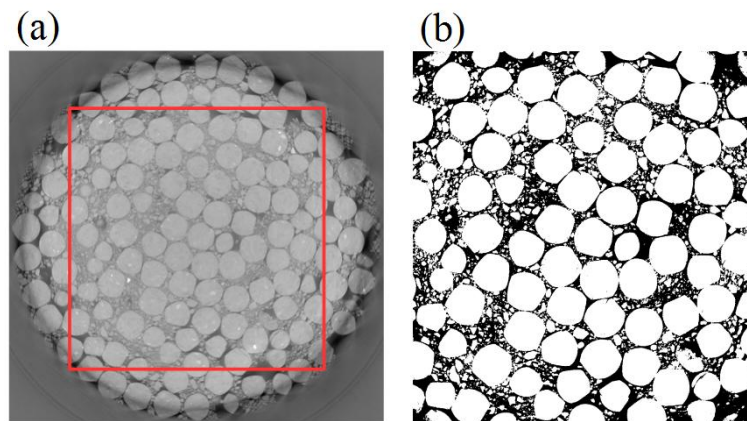
Figure 5. X-ray computed microtomography ( $\mu$ -CT) observations - vertical sections - of a pellet of bentonite at initial state.



540

541 Figure 6. 3D rendering of a pellet of bentonite at initial state (a) and of the crack network in a  
542 region of interest (b).

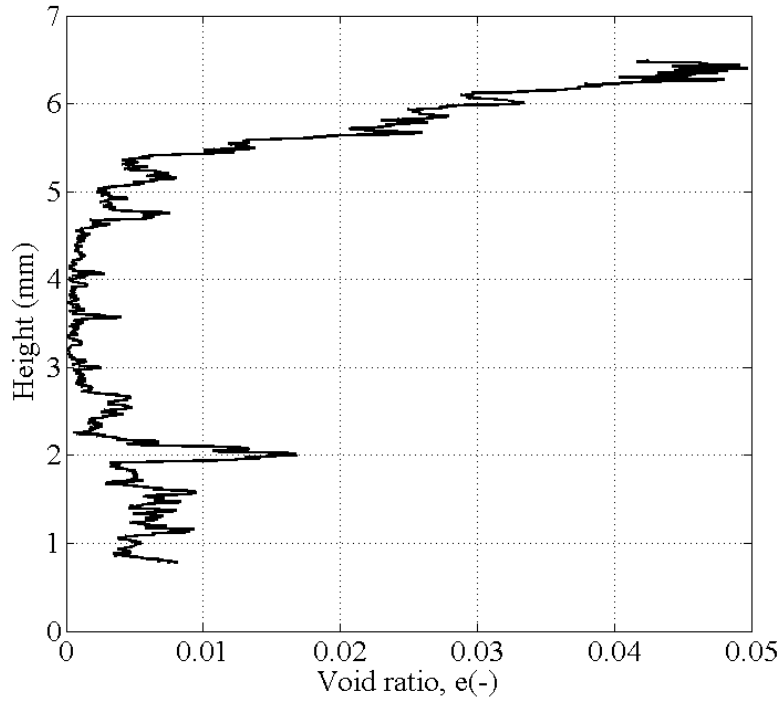
543



544

545 Figure 7. Horizontal slice with the selected ROI (a) and segmented image (b).





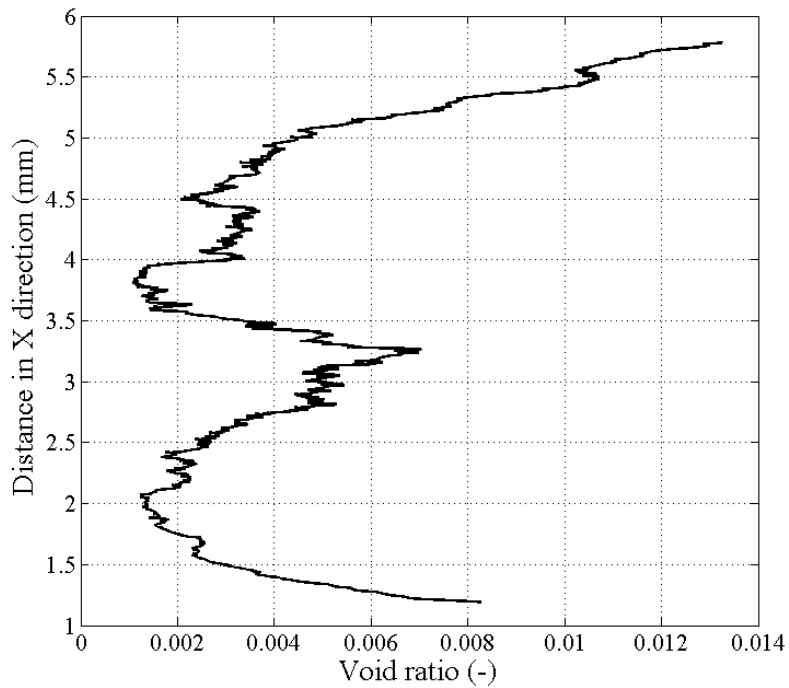
546

547

548

549

Figure 8. Evolution of the void ratio with height of a pellet of bentonite at initial state (Y direction – horizontal sections).



550

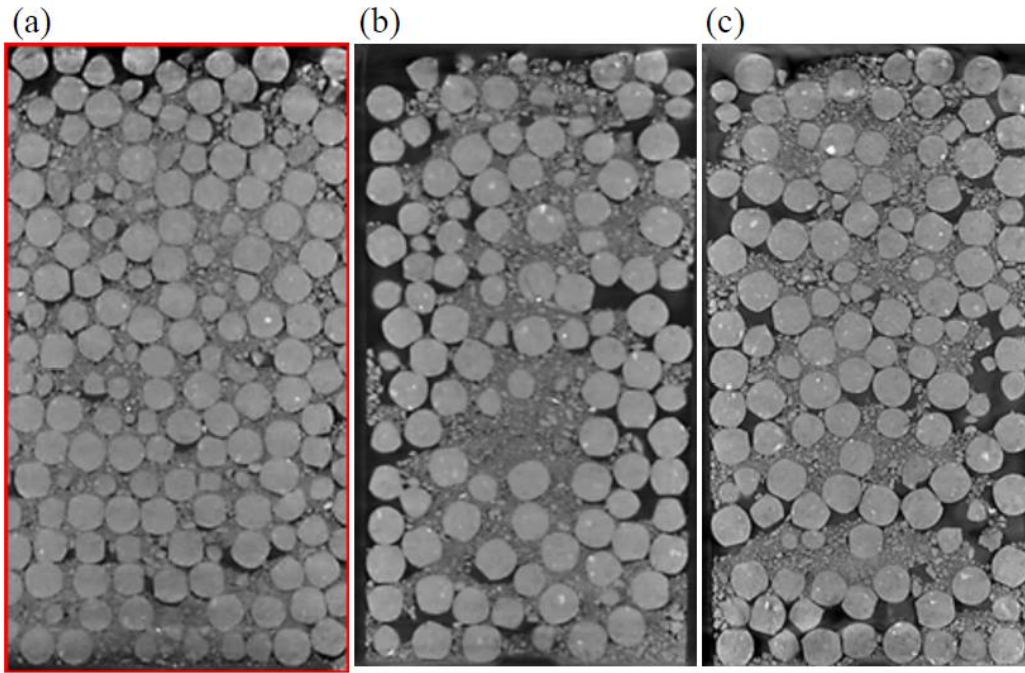
551

552

553

554

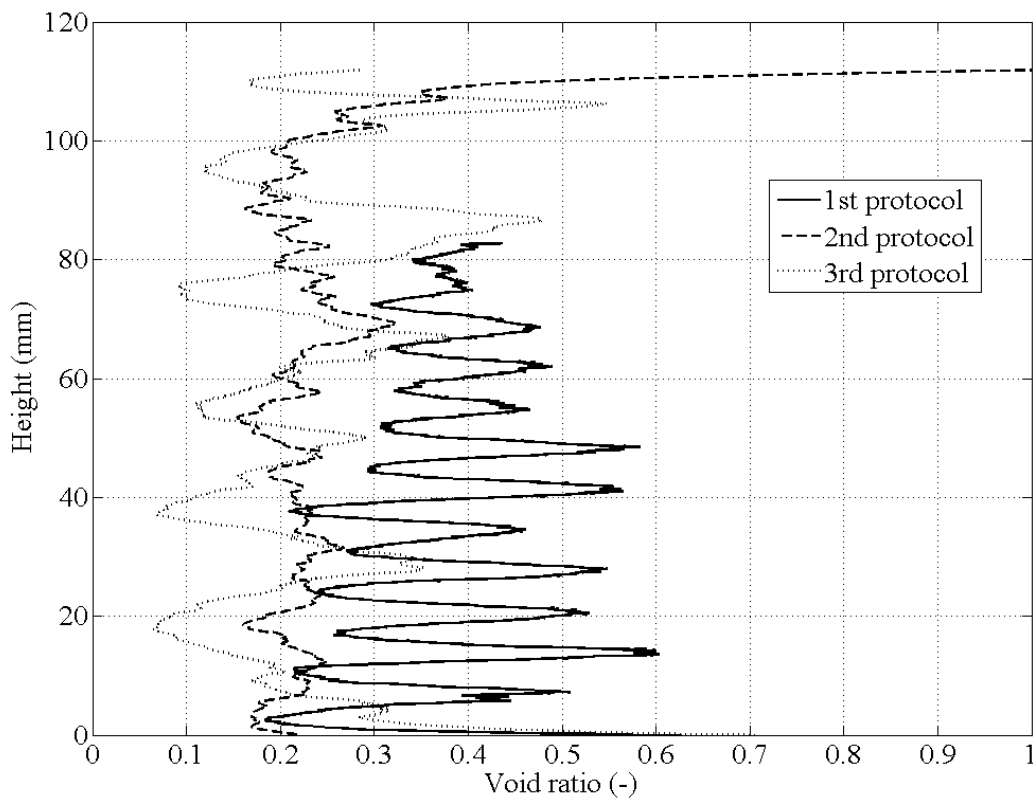
Figure 9. Evolution of the void ratio of a pellet of bentonite at initial state (X direction – vertical sections).



555

556 Figure 10. Vertical cross section of X-ray computed microtomography images of a mixture of  
 557 powder/pellets of bentonite with a proportion of 20/80 in dry mass obtained by three different  
 558 protocols. (a) First protocol of mixture, (b) Second protocol and (c) third protocol.

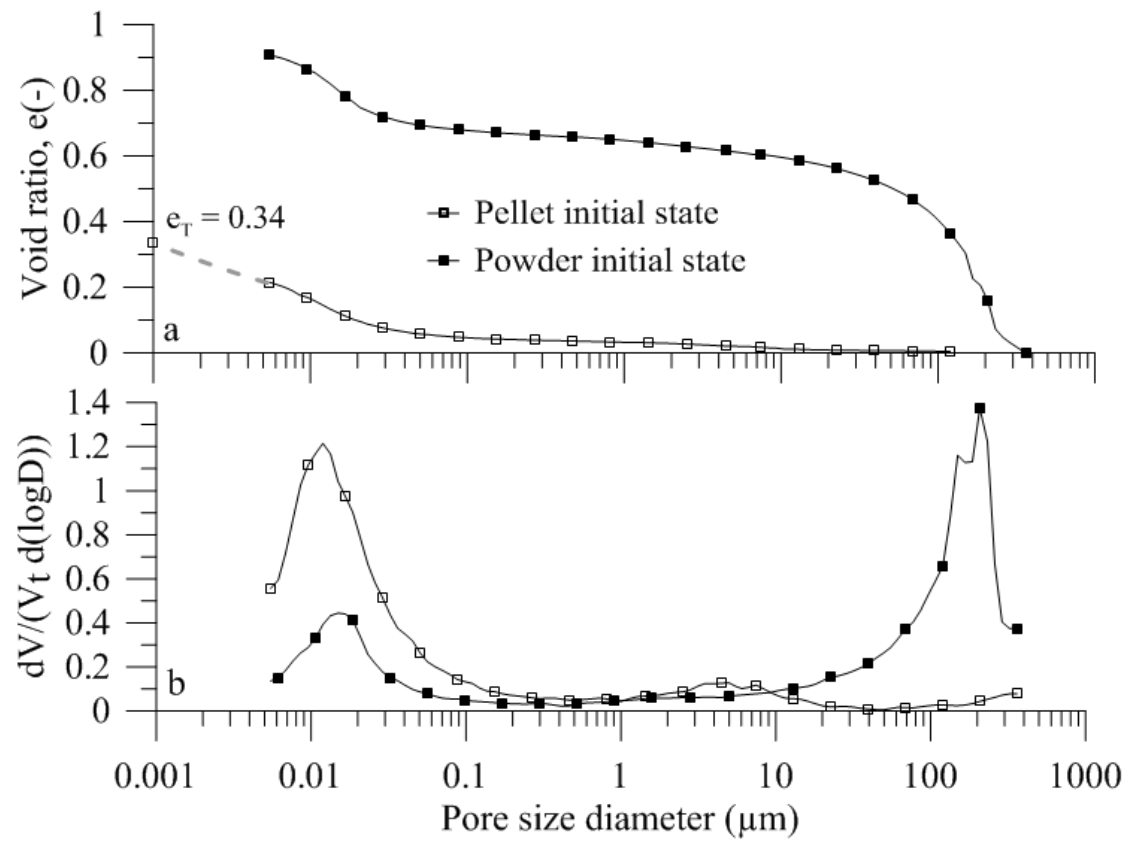
559



560

561 Figure 11. Evolution of the void ratio along height of a pellet/powder MX80 bentonite  
 562 mixture (80/20) fabricated by three protocols.

563



565

566 Figure 12. Cumulative porosity curve (a) and derivative curve (b) for a pellet and powder of  
 567 bentonite at their initial state.

568

569

570

571

572

573

574

575

576

577

578

579

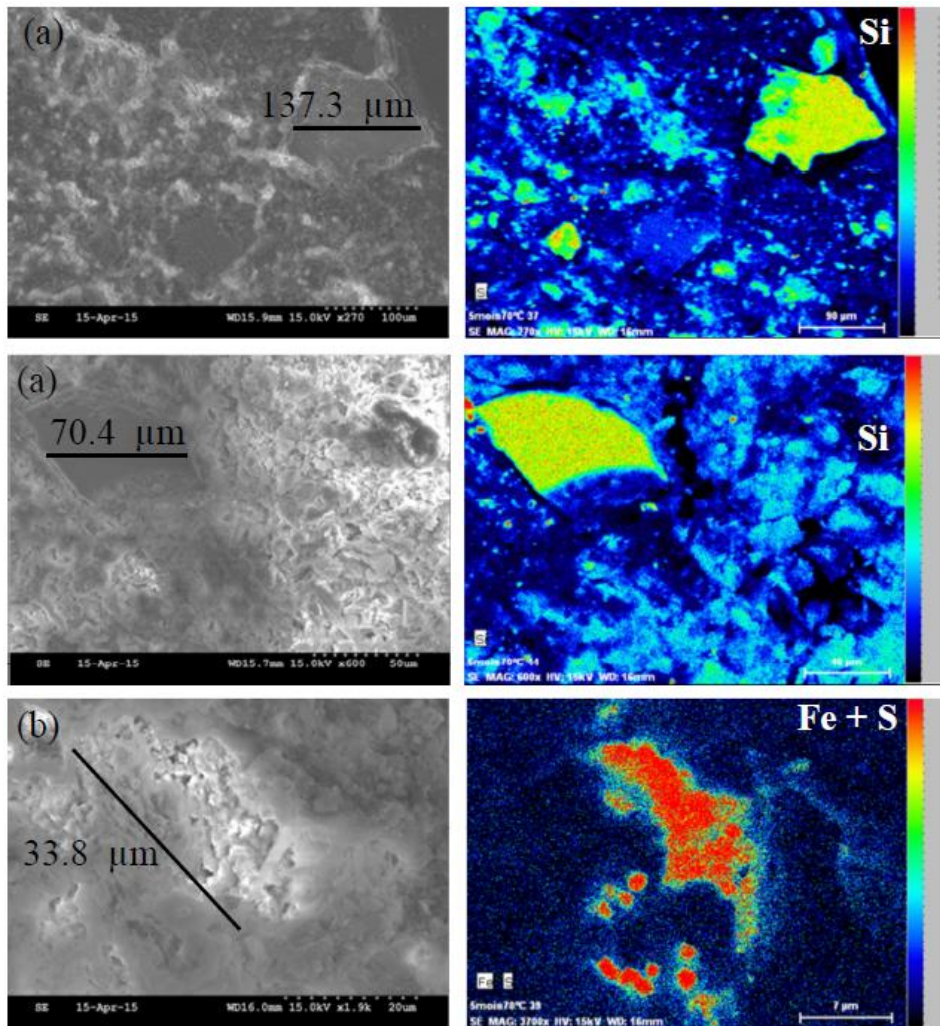


Figure 13. SEM pictures taken on a pellet of bentonite at its initial state (132.38 MPa of suction) + EDS results. Mineral inclusions of quartz (a, b) and pyrite (c). Dry unit mass  $\rho_d = 2.12 \text{ Mg/m}^3$

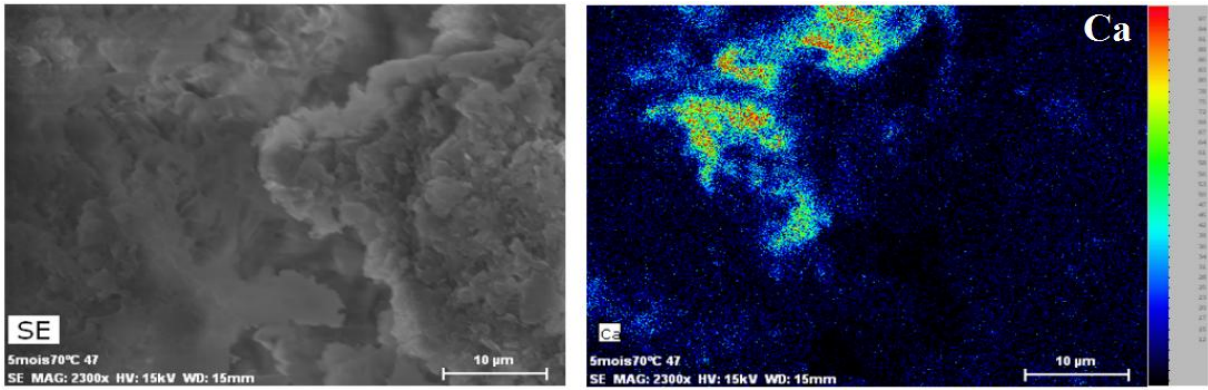


Figure 14. SEM picture taken on a pellet of bentonite at its initial state (132.38 MPa of suction) + EDS results. Mineral inclusion of calcite. Dry unit mass  $\rho_d = 2.12 \text{ Mg/m}^3$